$BaTiO_3$ Supercages: Unusual Oriented Nanoparticle Aggregation and Continuous Ordering Transition in Morphology

Juan Li,[†] Sami Hietala,[‡] and Xuelin Tian*[,§,∥]

[†]Department of Materials Science and Engineering, Aalto University, Espoo 02150, Finland, [‡]Laboratory of Polymer Chemistry, Department of Chemistry, University of Helsinki, P.O. Box 55, FIN 00014 Helsinki, Finland, [§]Department of Applied Physics, Aalto University, Espoo 02150, Finland, and [∥]Xinjiang Technical Institute of Physics and Chemistry, Chinese Academy of Sciences, Urumqi 830011, China

ABSTRACT Here we report the organic-free mesocrystalline superstructured cages of $BaTiO_3$, *i.e.*, the $BaTiO_3$ supercages, which are synthesized by a one-step templateless and additive-free route using molten hydrated salt as the reaction medium. An unusual three-dimensional oriented aggregation of primary $BaTiO_3$ nanoparticles in the medium of high ionic strength, which normally favors random aggregation, is identified to take place at the early stage of the synthesis. The spherical $BaTiO_3$ aggregates further experience a remarkable continuous ordering transition in morphology, consisting of nanoparticle faceting and nanosheet formation steps. This ordering transition in conjunction with Ostwald ripening-induced solid evacuation leads to the formation of unique supercage structure of $BaTiO_3$. Benefiting from their structure, the $BaTiO_3$ supercages exhibit improved microwave absorption property.

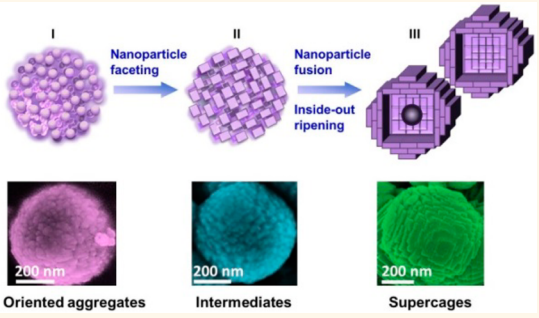

KEYWORDS: mesocrystals · hollow structures · oriented aggregation · electric double layer · ordering transition · molten hydrated salt · microwave absorption

Mesocrystals, comprising three-dimensional (3D) arrays of iso-oriented nanocrystallites, hold novel materials properties by combination of high crystallinity, subunit alignment and high porosity.[1−3] They also have important implications in the formation and artificial mimicking of biominerals, *e.g.*, nacre, sea urchin spines and sponge spicules.[4] Mesocrystal generation usually involves organic additives, which may temporarily stabilize the primary nanoparticles and prevent their uncontrolled and random aggregation, thus facilitating oriented assembly of nanoparticle into mesocrystals. Consequently, organic-free mesocrystals become challenging to synthesize.[5−7] On the other hand, nonspherical hollow structures have attracted enormous recent research interests because of their distinctive physicochemical properties,[8−13] whereas their preparation faces much more difficulties than common spherical hollow particles and often involves sacrificial self-templates and/or multistep processes. Here, we report one-step templateless and additive-free synthesis of organic-free mesocrystalline superstructured microcages (*i.e.*, supercages) of $BaTiO_3$, which consist of highly ordered layer-by-layer nanosheet assemblies and combine the desirable structural characteristics of mesocrystals and nonspherical micro/nanocages (Figure 1). The $BaTiO_3$ supercages, to the best of our knowledge, are the first report of organic-free, mesocrystalline and cage-like structure. Moreover, an unusual 3D oriented aggregation of primary nanoparticles is identified to take place in a reaction medium of high ionic strength, which normally promotes quick and random aggregation due to the electric double layer thinning effect.[14−16] The supercages are transformed from oriented nanoparticle aggregates through surface recrystallization coupled with Ostwald ripening-induced solid evacuation from the inner part of aggregates,

* Address correspondence to xuelin.tian@aalto.fi.

Received for review October 5, 2014 and accepted December 16, 2014.

Published online December 16, 2014
10.1021/nn505667x

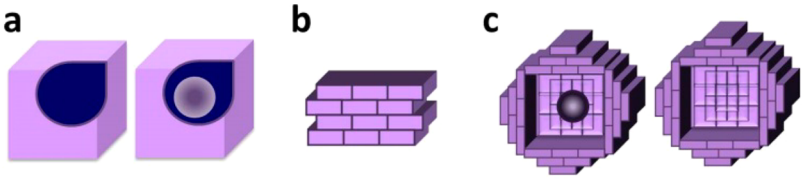

Figure 1. Schematic view of (c) mesocrystalline superstructured cages, which combine the structural characteristics of (a) hollow micro/nanocages and (b) mesocrystals of nanosheet assemblies.

and more interestingly, a continuous ordering transition in morphology from spherical aggregates to nearly cubic cages *via* nanoparticle faceting and nanosheet formation steps occurs during the synthesis. Benefiting from their unique mesocrystalline and cage-like structure, the $BaTiO_3$ supercages exhibit improved microwave absorption property compared with commercial $BaTiO_3$ nanopowder because of enhanced dielectric loss.

RESULTS AND DISCUSSION

Hydrated salts have been intensively studied as phase-change materials for heat management,[17,18] but their role in inorganic synthesis has been rarely explored.[19,20] In fact, molten hydrated salts (MHSs) can be an interesting type of solvent for dissolution of chemicals and implementation of chemical reactions. Compared with conventional water or organic solvents, the high polarity, high ionic strength and high viscosity of MHSs[21,22] could bring unique interaction with the dispersed chemicals, thus modifying their reactive behaviors and leading to products of novel structures. In this study, $BaTiO_3$ supercages were prepared through the reaction between TiO_2 and molten hydrated salt of $Ba(OH)_2 \cdot 8H_2O$ at 180 °C for 15 h, and the latter served as both the solvent and a reactant. The highly ordered superstructures of the $BaTiO_3$ supercages prepared at a lower filling rate differ markedly from previously reported hollow or core–shell $BaTiO_3$ particles,[19,20] which just showed spherical or less-ordered morphologies. It should be noted that the hydrated salt method employed here is different from conventional molten salt method, which uses molten anhydrous salt as a solvent and requires much higher reaction temperature, usually more than 400 °C and sometimes up to 1000 °C.[23–28] In contrast, our hydrated salt method can be operated at sufficiently lowered temperature (180 °C in this report) and is thus more energy-effective.

The X-ray powder diffraction (XRD, Figure 2a) pattern of the product can be indexed to perovskite $BaTiO_3$. Scanning electron microscopy (SEM, Figure 2b) investigation indicates the products are submicrometer particles (150–850 nm) possessing highly ordered hierarchical structures with cubic-like profile. What makes it more interesting is that the particles are composed of arrayed nanosheets with a thickness of 20–40 nm, which assemble in a layer-by-layer manner

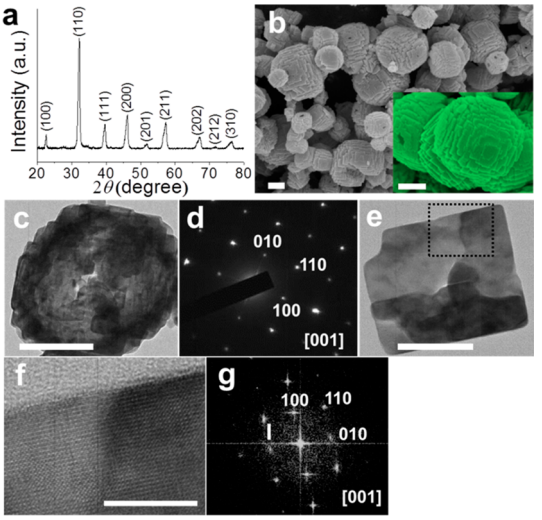

Figure 2. $BaTiO_3$ supercages prepared with a reaction time of 15 h. (a) XRD pattern, (b) SEM images, (c) TEM images, (d) ED pattern of the particle in (c), (e) TEM and (f) HRTEM images of a nanosheet detached from the supercages and (g) the FFT pattern of the nanosheet. Scale bars: (b and c) 200 nm, (e) 50 nm, and (f) 5 nm.

on the six faces of the cubic-like particles. Pores appearing on the surface suggest hollow interior of the products, which is confirmed by the SEM images of broken particles (Figure S1, Supporting Information). A thorough transmission electron microscopy (TEM, Figure 2c, and Figure S2, Supporting Information) examination indicates that the particles have either hollow or core–shell cage-like structures, and those less than 500 nm are always hollow whereas those larger than 500 nm usually show core–shell configuration. Layer-by-layer stacking of nanosheets on the cage shell can also be identified from the TEM images. Electron diffraction (ED, Figure 2d) analysis of the hollow cage gives nearly single-crystal diffraction pattern with some diffraction spots slightly elongated, revealing that the nanosheets are oriented in the same crystallographic direction, typical of mesocrystalline property. We further examined a single nanosheet detached from the cages, which shows nonuniform appearance and comprises several domains (Figure 2e), suggesting that the nanosheet formed through assembly and fusion of primary particles. High-resolution TEM (HRTEM, Figure 2f) and the corresponding fast Fourier transform (FFT, Figure 2g) analyses indicate the well crystallization of the nanosheet,

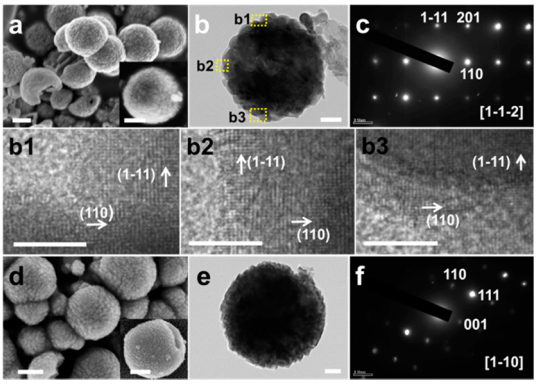

Figure 3. $BaTiO_3$ products prepared with different reaction times: (a–c) 3 h and (d–f) 5 h. (c) and (f) are the corresponding ED patterns of the particles shown in (b) and (e). (b1–b3) give the HRTEM images at different areas of the particle shown in (b). Scale bars: (a and d) 200 nm, (b and e) 50 nm, and (b1–b3) 5 nm.

which is oriented along the [001] zone axis. The above studies clearly verify that the products are highly ordered mesocrystalline superstructured cages, *i.e.*, supercages. As no organic additives or precursors were involved in the reaction, the products should be organic-free. The $BaTiO_3$ supercages shown here represent the first example of organic-free, mesocrystalline and cage-like structure.

To reveal the formation mechanism of the $BaTiO_3$ supercages, early stage products were investigated. XRD analyses indicate that TiO_2 transform to $BaTiO_3$ in no more than 3 h (Figure S3, Supporting Information). SEM and TEM investigations show that the products after reaction of 3 h are spherical aggregates consisting of primary nanoparticles with size between 15 and 40 nm (Figure 3a,b). ED analysis of the aggregate shown in Figure 3b gives a single crystal-like diffraction pattern (Figure 3c), although several very weak diffraction spots could not be indexed. This fact indicates that the primary nanoparticles are oriented in the same crystallographic direction in the early aggregates, which is further verified by detailed HRTEM examinations on different parts of the aggregate (Figure 3b1–b3).

With prolonged reaction time to 5 h, regular appearances instead of spherical ones begin to develop for the aggregates, and the constituent nanoparticles appear to be organized in a somewhat ordered and layer-by-layer manner, as highlighted by the SEM images (Figure 3d). The aggregation characteristic is also illustrated by SEM imaging of broken particles (Figure S4, Supporting Information). TEM analysis indicates that the nanoparticles at the surface are evolving into highly faceted crystallites at this stage (Figure 3e). HRTEM investigation provides further evidence on the faceting evolution of the constituent nanoparticles (Figure S5, Supporting Information). Consequently, the submicrometer aggregates begin to exhibit nonspherical and ordered profile. ED analysis shows a single crystal-like diffraction pattern (Figure 3f).

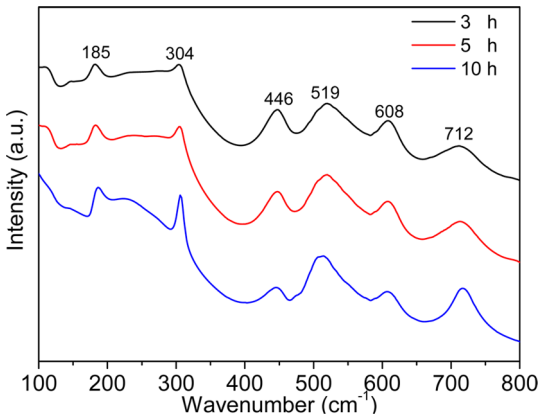

Figure 4. Raman spectra of the $BaTiO_3$ products prepared at different reaction time from 3, 5, to 10 h.

To further verify the crystallographic structure of the $BaTiO_3$ products, their Raman spectra were measured (Figure 4). Cubic $BaTiO_3$ has no inherent Raman active modes, whereas multiple characteristic modes are expected for noncentrosymmetric tetragonal $BaTiO_3$.[29–32] In our case, all the products, from 3 to 10 h, exhibit a peak at 304 cm^{-1}, which is a characteristic peak (B_1 mode) of tetragonal $BaTiO_3$ and indicates the asymmetry of TiO_6 octahedra.[29,30] The other peaks at 185, 519 (transverse optical mode of A_1 symmetry) and 712 (longitudinal optical mode of A_1 symmetry) cm^{-1} are also typical for tetragonal $BaTiO_3$. The attribution of peaks at 446 and 608 cm^{-1} is not clear yet, which is likely due to some local Ti–O framework similar to that of rutile.[33] The Raman results thus indicate the local noncentrosymmetric tetragonal characteristic of the $BaTiO_3$ products.

On the basis of the morphology and structure investigations of the products at different stages, the formation process of the $BaTiO_3$ supercages can be described as illustrated in Figure 5.

The highly alkaline reaction environment of molten $Ba(OH)_2 \cdot 8H_2O$ facilitates the transformation of TiO_2 precursor to $BaTiO_3$ through a dissolution–precipitation mechanism rather than an *in situ* topochemical process,[34] which is confirmed by the remarkable difference in size and morphology between the rutile precursor (Figure S6, Supporting Information) and $BaTiO_3$ products. Soluble Titanium species like $[Ti(OH)_x]^{4-x}$ form first through dissolution of TiO_2 in the alkaline medium, followed by a homogeneous nucleation of $BaTiO_3$ *via* the reaction between soluble titanium and barium sources.

Along with continuous nucleation and growth of $BaTiO_3$ nanoparticles, 3D oriented aggregation of primary nanoparticles takes place (Figure 5a,l, and Figure 3a–c). The occurrence of oriented aggregation in the MHS is highly interesting regarding the effect of ionic strength on nanoparticle aggregation. In a solution of high ionic strength, the electrical double layer (*i.e.*, surface charge and the associated counterion

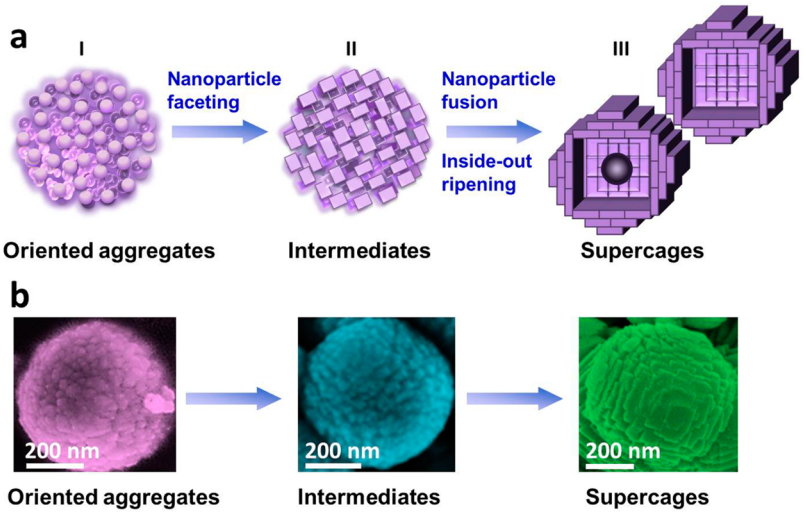

Figure 5. (a) Schematic illustration of the formation process of $BaTiO_3$ supercages. (b) SEM images showing the morphology transition process.

charge) around a nanoparticle is compressed due to the strong Debye screening effect, and hence the electrostatic repulsive barrier between nanoparticles is largely suppressed, which can lead to quick and random aggregation of nanoparticles.[14−16] Consequently, low ionic strength is generally considered to be important to ensure ordered aggregation of nanoparticles as it allows the particles to realign themselves into mutual crystallographic direction before permanently fixed by formation of strong chemical bonds. Compared to conventional aqueous solutions, the molten $Ba(OH)_2 \cdot 8H_2O$ has a drastically high ionic strength, and thus random aggregation would be expected, contrasting the practical fact. The unique physicochemical properties of the MHS thus should play important roles in the aggregation behavior of primary $BaTiO_3$ nanoparticles. We suggest the following factors may contribute to the oriented aggregation: (1) the high polarity (*i.e.*, alkalinity) and high ionic strength of the molten $Ba(OH)_2 \cdot 8H_2O$ lead to low MHS-oxide nanoparticle interfacial tension,[35] which temporarily stabilize the primary nanoparticles, preventing their uncontrolled and random aggregation; (2) the high viscosity of MHS[22] decreases the mobility of nanoparticles and also makes it more difficult to exclude the adsorbed MHS species between the nanoparticles during their aggregation and fusion, allowing more time and space for nanoparticle to adjust their orientation before permanently fixed. The viscosity of molten $Ba(OH)_2 \cdot 8H_2O$ is much higher than that of common solvents like water (Figure S7, Supporting Information). For example, its viscosity is 2 orders of magnitude higher than water at around 80 °C (0.1065 *vs* 0.000354 Pa·s). The above factors therefore counteract the effect of electric double layer thinning, and ensure sufficient freedom for nanoparticle realignment to the same crystallographic direction, minimizing the overall free energy of the system. The intrinsic dipole of tetragonal $BaTiO_3$ can assist the nanoparticles to orient themselves through interparticle dipole−dipole interaction, which is known to facilitate particle-interaction controlled oriented attachment and favors formation of complex superstructures.[36,37]

With prolonged reaction time, driven by further reduction of system free energy, the nanoparticles at the surface of the aggregates evolve into faceted morphologies, which should be bound by low energy faces like {100} faces (Figure 5a, II, and Figure 3d−f). Further MHS treatment leads to fusion and growth of the faceted nanocrystallites into nanosheets, and at the same time, cage-like structures develop through Ostwald ripening-induced solid evacuation from the inner part of aggregates, giving the formation of $BaTiO_3$ supercages (Figure 5a, III, and Figure 2). Ostwald ripening is a well-known route for formation of hollow structures from solid aggregates of nanoparticles.[38] The inner nanoparticles form at earlier stages of nucleation and growth than the outer nanoparticles, which could lead to smaller inner nanoparticles and relatively larger outer nanoparticles. This may cause the preferential dissolution and outward diffusion of nanoparticles from the inner part through Ostwald ripening. The residual electrostatic repulsion between nanoparticles might also play a minor role by facilitating formation of a loosely packed inner part.[39] Note that steps II and III do not separate completely, and Ostwald ripening involves in both steps, providing substance for surface recrystallization. The formation of $BaTiO_3$ supercages *via* continuous morphology transition is also depicted by SEM images in Figure 5b.

Additionally, we found that when prolonging the reaction time to 20 h, the $BaTiO_3$ supercages could eventually transform into nearly cubic cages with single crystal-like shell (Figure 6), attributed to further fusion and growth of nanosheets. Note that the cages

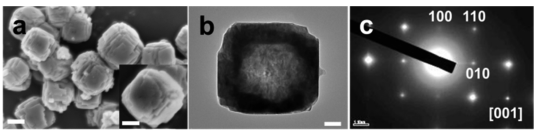

Figure 6. (a) SEM, (b) TEM and (c) ED pattern of $BaTiO_3$ products prepared with reaction time of 20 h. Scale bars: (a) 200 nm and (b) 50 nm.

formed at this stage include both hollow and core–shell structures (Figure S9, Supporting Information), similar to the situation of products obtained after reaction for 15 h. Therefore, our study also provides a comprehensive picture of continuous ordering transition in morphology from irregular spherical aggregates to cubic single crystal-like cages *via* nanoparticle faceting, nanosheet formation and further fusion steps. The oriented aggregation of the initial nanoparticles is important for the continuous morphology transition as it allows easy fusion between nanoparticles and nanosheets that have aligned in the same crystallographic direction.

As a typical dielectric material with relaxation occurring at gigahertz (GHz) frequencies, $BaTiO_3$ is potentially useful for microwave absorption.[40−43] The unique structure of the $BaTiO_3$ supercages is interesting for investigation of this property: The cage configuration and mesocrystalline substructures of high interfacial areas increase possibility of multireflection and interfacial polarization relaxation loss; hollow interior also facilitates gain of lightweight microwave absorption materials. Figure 7a shows the real (ε') and imaginary (ε'') parts of complex permittivity, and the real (μ') and imaginary (μ'') parts of complex permeability of the $BaTiO_3$ supercage–paraffin (w/w = 7:3) composite in the frequency range of 2−18 GHz. The reflection loss (RL) of the composite was then calculated using the transmission line theory:[44]

$$Z_{in} = Z_0(\mu/\varepsilon)^{1/2}\tanh[j(2\pi fd/c)(\mu\varepsilon)^{1/2}] \quad (1)$$

$$RL = 20\log|(Z_{in} - Z_0)/(Z_{in} + Z_0)| \quad (2)$$

where Z is the input impedance of the absorber, Z_0 the impedance of free space, f the frequency of microwave, d the thickness of the absorber and c the velocity of light. Figure 7b shows the RL of the supercage–paraffin composite, indicating effective absorption in the high frequency region (13−18 GHz). As the imaginary permeability μ'' is nearly zero in the whole frequency range, the RL is mainly attributed to the dielectric loss. The imaginary permittivity ε'' becomes negative in the high

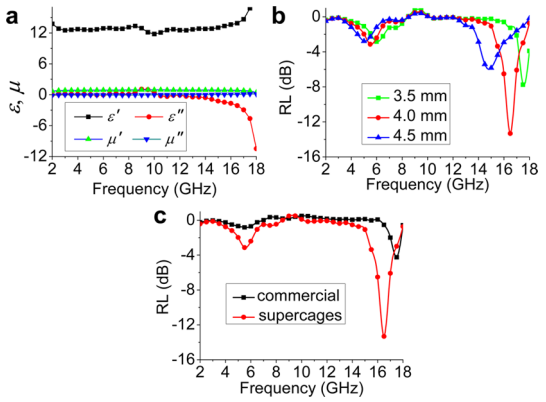

Figure 7. (a) Complex permittivity (ε) and permeability (μ) of the $BaTiO_3$ supercage–paraffin composite, (b) reflection loss (RL) of the $BaTiO_3$ supercages–paraffin composite of different thicknesses, and (c) comparison of RL between the $BaTiO_3$ supercages–paraffin composite and commercial $BaTiO_3$ nanoparticle–paraffin composite with a thickness of 4 mm.

frequency region, which is due to that the dipole polarization cannot keep up with the rapidly varying electromagnetic field, thus leading to a negative phase angle. The remarkable ε'' values at high frequencies facilitate large dielectric loss and thus give high RL of the supercage–paraffin composite. For comparison, a composite made of commercial $BaTiO_3$ nanoparticles (size of 100−500 nm, Figure S10, Supporting Information) and paraffin (w/w = 7:3) shows limited ε'' values and consequently much weaker RL (Figure 7c and Figure S11, Supporting Information). These results verify that the $BaTiO_3$ supercage structure benefits microwave absorption through enhanced dielectric loss.

CONCLUSIONS

In summary, highly ordered, organic-free and mesocrystalline $BaTiO_3$ supercages are facilely synthesized, which evolves from the 3D oriented aggregates of primary nanoparticles in MHS medium. A continuous ordering transition in morphology from spherical aggregates to nearly cubic cages *via* nanoparticle faceting and nanosheet formation steps is revealed. Low MHS-oxide interfacial tension and high viscosity of the MHS are suggested to temporarily stabilize the primary nanoparticles and prevent their quick and random aggregation, thus facilitating the oriented aggregation of nanoparticles. Due to their unique physicochemical characteristics, MHSs may serve as a useful system for investigating nanoparticle aggregation and for preparing novel inorganic superstructures with improved properties.

METHODS

Synthesis of $BaTiO_3$ Supercages. A total of 1.5 g of $Ba(OH)_2 \cdot 8H_2O$ (mp 78 °C) was melted above its melting point. Then 0.1 g of rutile TiO_2 powder (size: 0.6−4 μm, Supporting Information, Figure S6) was added to the MHS of $Ba(OH)_2 \cdot 8H_2O$, which was stirred by a Teflon stick for a few seconds to give uniform dispersion of TiO_2. The mixture was sealed in a 23 mL Teflon-lined autoclave and kept at 180 °C for 15 h. After being cooled to room temperature, the obtained solid was thoroughly washed

with dilute acetic acid and water, and then dried at ambient conditions for further characterizations. Incidentally, we found that $BaTiO_3$ nanocubes with size of tens of nanometers coexisted with the supercage products, which might be evolved from nonaggregated primary nanoparticles dispersed in the MHS medium (Figure S8, Supporting Information). It was found that the filling rate affected the morphologies of the products markedly, and a high filling rate (*e.g.*, 3 g of MHS and 0.2 g of TiO_2) would lead to $BaTiO_3$ products of less-ordered morphologies without layered structure. This may be caused by the deposition of the formed $BaTiO_3$ nanoparticles at the bottom of the autoclave, and high filling rate leads to deposition of more nanoparticles there within a certain period, thus giving uncontrolled and less-ordered aggregation of nanoparticles.

Characterization. Crystallographic phase was investigated by X-ray powder diffraction (XRD, Bruker D8 Advance, Cu Kα, λ = 1.5418 Å). The morphology and structure were characterized by scanning electron microscope (SEM, JEOL JSM-6700F) and transmission electron microscope (TEM, JEOL JEM-2010). Raman spectra were obtained on a Bruker Vertex 70 RAMII FT-Raman spectrometer, equipped with liquid nitrogen cooled Germanium detector and Nd:YAG laser excitation at 1064 nm in a spectral resolution of 4 cm^{-1}. Viscosity of $Ba(OH)_2 \cdot 8H_2O$ was determined by a TA Instruments AR2000 stress-controlled rheometer equipped with a 20 mm plate geometry. The salt was heated quickly above the melting point (78 °C) and flow viscosity at a shear rate of 100 s^{-1} was measured at increasing the temperature from 80 °C at a heating rate of 1 °C/min. Steady decrease of viscosity upon heating was observed until to 87 °C. Above 87 °C, the loss of water of hydration leads to increase in the observed viscosity and finally to crystallization of the dehydrated salt. The prediction of flow viscosities at higher temperatures were then obtained by extrapolation of the decreasing viscosity assuming an Arrhenius-type flow behavior. The detailed viscosity data is provided in the Supporting Information (Figure S7). To measure the complex permittivity and complex permeability, the $BaTiO_3$ supercages or commercial nanoparticles (purchased from Shanghai Aladdin Chemicals, China) were dispersed into paraffin wax with a weight fraction of 70%, and the mixture was pressed into toroidal sample (outer diameter, 7 mm; inner diameter, 3 mm, and thickness, 2 mm). The complex permittivity and permeability were then measured using a XMKJ-AV3627 vector network analyzer in the frequency range of 2−18 GHz.

Conflict of Interest: The authors declare no competing financial interest.

Acknowledgment. We thank the support from the Academy of Finland (Centres of Excellence Programme (2014−2019)) and National Natural Science Foundation of China (No. 21101167). We thank Dr. K. Chen, Prof. Z. Zhou, Dr. X. Wang, and Dr. P. Hiekkataipale for experimental help and valuable discussions.

Supporting Information Available: More SEM and TEM images of $BaTiO_3$ products after reaction for 5, 15, and 20 h, XRD of products after reaction for 3, 5, and 20 h, XRD and SEM analyses of TiO_2 precursor and commercial $BaTiO_3$ nanoparticles, viscosity data of $Ba(OH)_2 \cdot 8H_2O$ at different temperatures, microwave absorption property of commercial $BaTiO_3$ nanoparticle-paraffin composite. This material is available free of charge *via* the Internet at http://pubs.acs.org.

REFERENCES AND NOTES

1. Cölfen, H.; Antonietti, M. Mesocrystals: Inorganic Superstructures Made by Highly Parallel Crystallization and Controlled Alignment. *Angew. Chem., Int. Ed.* **2005**, *44*, 5576–5591.
2. Meldrum, F. C.; Cölfen, H. Controlling Mineral Morphologies and Structures in Biological and Synthetic Systems. *Chem. Rev.* **2008**, *108*, 4332–4432.
3. Song, R.-Q.; Cölfen, H. Mesocrystals-Ordered Nanoparticle Superstructures. *Adv. Mater.* **2010**, *22*, 1301–1330.
4. Oaki, Y.; Kotachi, A.; Miura, T.; Imai, H. Bridged Nanocrystals in Biominerals and Their Biomimetics: Classical yet Modern Crystal Growth on the Nanoscale. *Adv. Funct. Mater.* **2006**, *16*, 1633–1639.
5. Ye, J.; Liu, W.; Cai, J.; Chen, S.; Zhao, X.; Zhou, H.; Qi, L. Nanoporous Anatase TiO_2 Mesocrystals: Additive-Free Synthesis, Remarkable Crystalline-Phase Stability, and Improved Lithium Insertion Behavior. *J. Am. Chem. Soc.* **2010**, *133*, 933–940.
6. Fang, J.; Ding, B.; Gleiter, H. Mesocrystals: Syntheses in Metals and Applications. *Chem. Soc. Rev.* **2011**, *40*, 5347–5360.
7. Hong, Z.; Wei, M.; Lan, T.; Jiang, L.; Cao, G. Additive-Free Synthesis of Unique TiO_2 Mesocrystals with Enhanced Lithium-Ion Intercalation Properties. *Energy Environ. Sci.* **2012**, *5*, 5408–5413.
8. Yin, Y. D.; Rioux, R. M.; Erdonmez, C. K.; Hughes, S.; Somorjai, G. A.; Alivisatos, A. P. Formation of Hollow Nanocrystals through the Nanoscale Kirkendall Effect. *Science* **2004**, *304*, 711–714.
9. Yang, H. G.; Zeng, H. C. Self-Construction of Hollow SnO_2 Octahedra Based on Two-Dimensional Aggregation of Nanocrystallites. *Angew. Chem., Int. Ed.* **2004**, *43*, 5930–5933.
10. Wang, L.; Tang, F.; Ozawa, K.; Chen, Z.-G.; Mukherj, A.; Zhu, Y.; Zou, J.; Cheng, H.-M.; Lu, G. Q. A General Single-Source Route for the Preparation of Hollow Nanoporous Metal Oxide Structures. *Angew. Chem., Int. Ed.* **2009**, *48*, 7048–7051.
11. Yang, X. F.; Fu, J. X.; Jin, C. J.; Chen, J. A.; Liang, C. L.; Wu, M. M.; Zhou, W. Z. Formation Mechanism of $CaTiO_3$ Hollow Crystals with Different Microstructures. *J. Am. Chem. Soc.* **2010**, *132*, 14279–14287.
12. Zhang, L.; Zhou, L.; Wu, H. B.; Xu, R.; Lou, X. W. Unusual Formation of Single-Crystal Manganese Sulfide Microboxes Co-Mediated by the Cubic Crystal Structure and Shape. *Angew. Chem., Int. Ed.* **2012**, *51*, 7267–7270.
13. Zhao, Y.; Jiang, L. Hollow Micro/Nanomaterials with Multilevel Interior Structures. *Adv. Mater.* **2009**, *21*, 3621–3638.
14. Soare, L. C.; Bowen, P.; Lemaitre, J.; Hofmann, H. Precipitation of Nanostructured Copper Oxalate: Substructure and Growth Mechanism. *J. Phys. Chem. B* **2006**, *110*, 17763–17771.
15. Collier, A. P.; Hetherington, C. J. D.; Hounslow, M. J. Alignment Mechanisms between Particles in Crystalline Aggregates. *J. Cryst. Growth* **2000**, *208*, 513–519.
16. Burrows, N. D.; Hale, C. R. H.; Penn, R. L. Effect of Ionic Strength on the Kinetics of Crystal Growth by Oriented Aggregation. *Cryst. Growth Des.* **2012**, *12*, 4787–4797.
17. Voigt, W.; Zeng, D. Solid-Liquid Equilibria in Mixtures of Molten Salt Hydrates for the Design of Heat Storage Materials. *Pure Appl. Chem.* **2002**, *74*, 1909–1920.
18. Hyun, D. C.; Levinson, N. S.; Jeong, U.; Xia, Y. Emerging Applications of Phase-Change Materials (Pcms): Teaching an Old Dog New Tricks. *Angew. Chem., Int. Ed.* **2014**, *53*, 3780–3795.
19. Tian, X.; Li, J.; Chen, K.; Han, J.; Pan, S. Template-Free and Scalable Synthesis of Core−Shell and Hollow $Batio_3$particles: Using Molten Hydrated Salt as a Solvent. *Cryst. Growth Des.* **2009**, *9*, 4927–4932.
20. Tian, X. L.; Li, J. A.; Chen, K.; Han, J. A.; Pan, S. L.; Wang, Y. J.; Fan, X. Y.; Li, F.; Zhou, Z. X. Nearly Monodisperse Ferroelectric $Batio_3$ Hollow Nanoparticles: Size-Related Solid Evacuation in Ostwald-Ripening-Lnduced Hollowing Process. *Cryst. Growth Des.* **2010**, *10*, 3990–3995.
21. Angell, C. A. Electrical Conductance of Concentrated Aqueous Solutions and Molten Salts—Correlation through Free Volume Transport Model. *J. Phys. Chem.* **1965**, *69*, 2137–2137.
22. Jain, S. K. Density, Viscosity, and Surface Tension of Some Single Molten Hydrated Salts. *J. Chem. Eng. Data* **1978**, *23*, 170–173.
23. Mao, Y. B.; Banerjee, S.; Wong, S. S. Large-Scale Synthesis of Single-Crystalline Perovskite Nanostructures. *J. Am. Chem. Soc.* **2003**, *125*, 15718–15719.
24. Wang, W. Z.; Xu, C. K.; Wang, G. H.; Liu, Y. K.; Zheng, C. L. Preparation of Smooth Single-Crystal Mn_3O_4 Nanowires. *Adv. Mater.* **2002**, *14*, 837–840.

25. Xu, C.-Y.; Zhen, L.; Yang, R.; Wang, Z. L. Synthesis of Single-Crystalline Niobate Nanorods *via* Ion-Exchange Based on Molten-Salt Reaction. *J. Am. Chem. Soc.* **2007**, *129*, 15444–15445.
26. Tian, Y.; Chen, D. R.; Jiao, X. L.; Duan, Y. Z. Facile Preparation and Electrochemical Properties of Cubic-Phase $Li_4Mn_5O_{12}$ Nanowires. *Chem. Commun.* **2007**, 2072–2074.
27. Chen, H. L.; Grey, C. P. Molten Salt Synthesis and High Hate Performance of the "Desert-Rose" Form of $LiCoO_2$. *Adv. Mater.* **2008**, *20*, 2206–2210.
28. Xu, T.; Zhou, X.; Jiang, Z. Y.; Kuang, Q.; Xie, Z. X.; Zheng, L. S. Syntheses of Nano/Submicrostructured Metal Oxides with All Polar Surfaces Exposed *via* a Molten Salt Route. *Cryst. Growth Des.* **2009**, *9*, 192–196.
29. Asiaie, R.; Zhu, W.; Akbar, S. A.; Dutta, P. K. *Chem. Mater.* **1996**, *8*, 226–234.
30. Moreira, M. L.; Mambrini, G. P.; Volanti, D. P.; Leite, E. R.; Orlandi, M. O.; Pizani, P. S.; Mastelaro, V. R.; Paiva-Santos, C. O.; Longo, E.; Varela, J. A. Hydrothermal Microwave: A New Route to Obtain Photoluminescent Crystalline $BatiO_3$ Nanoparticles. *Chem. Mater.* **2008**, *20*, 5381–5387.
31. Niederberger, M.; Pinna, N.; Polleux, J.; Antonietti, M. A General Soft-Chemistry Route to Perovskites and Related Materials: Synthesis of $BatiO_3$, $BaZrO_3$, and $LiNbO_3$ Nanoparticles. *Angew. Chem., Int. Ed.* **2004**, *43*, 2270–2273.
32. Gao, Y.; Shvartsman, V. V.; Elsukova, A.; Lupascu, D. C. Low-Temperature Synthesis of Crystalline $BaTiO_3$ Nanoparticles by One-Step "Organosol"-Precipitation. *J. Mater. Chem.* **2012**, *22*, 17573–17583.
33. Porto, S. P. S.; Fleury, P. A.; Damen, T. C. Raman Spectra of TiO_2, MgF_2,ZnF_2,FeF_2, and MnF_2. *Phys. Rev.* **1967**, *154*, 522–526.
34. Maxim, F.; Ferreira, P.; Vilarinho, P. M.; Reaney, I. Hydrothermal Synthesis and Crystal Growth Studies of $BaTiO_3$ Using Ti Nanotube Precursors. *Cryst. Growth Des.* **2008**, *8*, 3309–3315.
35. Vayssieres, L.; Hagfeldt, A.; Lindquist, S. E. Purpose-Built Metal Oxide Nanomaterials. The Emergence of a New Generation of Smart Materials. *Pure Appl. Chem.* **2000**, *72*, 47–52.
36. Dalmaschio, C. J.; Ribeiro, C.; Leite, E. R. Impact of the Colloidal State on the Oriented Attachment Growth Mechanism. *Nanoscale* **2010**, *2*, 2336–2345.
37. Yasui, K.; Kato, K. Dipole−Dipole Interaction Model for Oriented Attachment of $BaTiO_3$ Nanocrystals: A Route to Mesocrystal Formation. *J. Phys. Chem. C* **2011**, *116*, 319–324.
38. Yec, C. C.; Zeng, H. C. Synthesis of Complex Nanomaterials *via* Ostwald Ripening. *J. Mater. Chem. A* **2014**, *2*, 4843–4861.
39. Xia, Y.; Nguyen, T. D.; Yang, M.; Lee, B.; Santos, A.; Podsiadlo, P.; Tang, Z.; Glotzer, S. C.; Kotov, N. A. Self-Assembly of Self-Limiting Monodisperse Supraparticles from Polydisperse Nanoparticles. *Nat. Nanotechnol.* **2011**, *6*, 580–587.
40. Zhu, Y. F.; Zhang, L.; Natsuki, T.; Fu, Y. Q.; Ni, Q. Q. Facile Synthesis of $BaTiO_3$ Nanotubes and Their Microwave Absorption Properties. *ACS Appl. Mater. Interfaces* **2012**, *4*, 2101–2106.
41. Yang, J.; Zhang, J.; Liang, C. Y.; Wang, M.; Zhao, P. F.; Liu, M. M.; Liu, J. W.; Che, R. C. Ultrathin $BaTiO_3$ Nanowires with High Aspect Ratio: A Simple One-Step Hydrothermal Synthesis and Their Strong Microwave Absorption. *ACS Appl. Mater. Interfaces* **2013**, *5*, 7146–7151.
42. Saini, P.; Arora, M.; Gupta, G.; Gupta, B. K.; Singh, V. N.; Choudhary, V. High Permittivity Polyaniline-Barium Titanate Nanocomposites with Excellent Electromagnetic Interference Shielding Response. *Nanoscale* **2013**, *5*, 4330–4336.
43. Jiang, J. J.; Li, D.; Geng, D. Y.; An, J.; He, J.; Liu, W.; Zhang, Z. D. Microwave Absorption Properties of Core Double-Shell FeCo/C/ $BaTiO_3$ Nanocomposites. *Nanoscale* **2014**, *6*, 3967–3971.
44. Matsumoto, M.; Miyata, Y. Thin Electromagnetic Wave Absorber for Quasi-Microwave Band Containing Aligned Thin Magnetic Metal Particles. *IEEE Trans. Magn.* **1997**, *33*, 4459–4464.